

# **Interfacial Shear Stress Transfer at Nanowire-Polymer Interfaces using in-situ Atomic Force Microscopy: Experiments and Modeling**

Felipe Robles Poblete and Yong Zhu\*

Department of Mechanical and Aerospace Engineering, North Carolina State University, Raleigh,  
North Carolina 27695

\* Corresponding author. E-mail address: [yong\\_zhu@ncsu.edu](mailto:yong_zhu@ncsu.edu) (Y. Zhu).

## **Abstract**

Interfacial mechanics between nanostructures and matrix is of critical importance for a range of device applications of the nanostructures. However, it is challenging to characterize interfacial shear stress transfer at such nanoscale interfaces. In this work, we report a new method to study the interfacial shear stress transfer of single Si nanowires on top of a polymer substrate that is subjected to uniaxial tensile loading. In-situ atomic force microscopy (AFM) testing is used to measure the nanowire deformation, more specifically, average axial strain, as a function of the applied strain to the substrate. Two types of substrates, as-prepared and chemically treated, are selected to examine the effect of van der Waals interactions and chemical bonding. It is found that nonlinear and bilinear cohesive shear-lag models can well capture the interfacial shear stress transfer characteristics associated with the two types of interactions, respectively. For each type, the interface parameters such as interfacial stiffness, shear strength, and/or fracture toughness are identified by fitting the experimental results. This work provides valuable insights into fundamental mechanisms underlying the interfacial shear-lag models. In addition, a parametric study with different nanowire dimensions is carried out, which can provide a guide to experimental design of elastic strain engineering and fracture of Si nanowires.

*Keywords: Interfacial shear stress; Shear-lag models; Cohesive zone modeling; van der Waals interactions; Chemical Bonding*

## **1. Introduction**

A plethora of nanomaterials with outstanding properties have emerged over the past decades. Among them, one-dimensional (1D) nanomaterials have been used as building blocks in a wide range of applications. Carbon nanotubes (CNTs) and nanowires has been widely used in flexible transparent electrodes and more recently stretchable electronics (Rogers et al., 2010; Yao and Zhu, 2015). CNTs and nanowires have also been used in nanocomposites showing enhanced mechanical properties (Coleman et al., 2006; Qian et al., 2002). Elastic strain engineering can be utilized to tune the fundamental properties of semiconductor materials. Bent or buckled nanowires constrained by a substrate showed considerable changes in electronic properties such as bandgap (Han et al., 2009). Moreover, transfer printing and alignment of semiconductor nanowires as the functional materials is important for their device applications (Xu et al., 2011a). For the applications mentioned above, among many others, interface mechanics between nanomaterials and the substrate (or matrix) is of critical relevance (Zhu, 2017).

There have been relatively few studies on the nanowire/substrate interfacial shear stress transfer. When the polymer substrate is compressed, the nanowire on top can buckle into either 2D (in-plane) wavy shape or 3D coiled shape, where interfacial shear stress plays a key role in regulating the buckling shape (Chen et al., 2016a, 2016b; Ryu et al., 2009; Xu et al., 2011b). In the case of Si nanowires on top of polydimethylsiloxane (PDMS) substrate, ultraviolet-ozone (UVO) treatment of the substrate can lead to different buckling shapes. Xu et al. found that with increasing UVO time, the buckling shape of the Si nanowires transits between the 2D wavy and

the 3D coil shape (Xu et al., 2011b). UVO treatment can change the bonding type between Si nanowire and PDMS and effectively tune the adhesion and interfacial shear strength.

It is challenging to measure interfacial shear strength between nanowire and substrate. One method is pull-out of a single nanowire or CNT from the matrix (Chen et al., 2015; Ding et al., 2003). Due to the small size of nanowires, the pull-out test is typically performed inside a scanning electron microscope (SEM). For a non-conductive matrix and/or nanowire, electron beam can cause formation of electron double layers at the nanowire-matrix interface (Miyazaki et al., 2000), leading to extra electrostatic force. Another method recently developed for 1D nanomaterials is based on so-called “the most-bent state” (Hou et al., 2015; Qin and Zhu, 2011; Strus et al., 2009). A single nanowire on a substrate is bent to the most bent state using an atomic force microscope (AFM) tip (Strus et al., 2009) or a manipulator tip under optical microscope (Hou et al., 2015; Qin and Zhu, 2011); the most bent state is a critical state, beyond which the nanowire would relax upon removing of the AFM or manipulator tip. From the nanowire profile at the critical state the interfacial shear strength can be determined. However, this method involves third-order differentiation of the nanowire profile, which can introduce large errors. Furthermore, this method can only provide the shear strength without providing other interface parameters such as the energy and range of the interaction.

Single-fiber fragmentation is among the major methods to characterize mechanical behavior of the microfiber/matrix interface in composites (Drzal and Madhukar, 1993; Wagner and Eitan, 1990). In this method, a microfiber is embedded in a matrix coupon. With increasing load applied to the matrix, the fiber eventually breaks in the matrix as a result of interfacial shear stress transfer. This fragmentation process is repeated producing shorter and shorter fragments until the remaining fragments are no longer sufficient in length to further fracture. With the final

fiber length-to-diameter ratio measured, a shear-lag model analysis can be conducted to calculate the interfacial shear strength. It would be of interest to explore this method to investigate the behavior at the nanowire/polymer interfaces. Compared to the microfibers used in the fragmentation method, nanowires are much shorter and thinner (typically  $\sim 10\ \mu\text{m}$  in length and  $< 100\ \text{nm}$  in diameter). Due to their short length, however, it would be difficult to fragment the nanowires. Therefore, a new method to measure the nanowire deformation as well as interpret the measurement data must be developed. On the other hand, due to their small diameter, it might be possible to place the nanowires on top of a substrate, instead of inside a matrix, which can facilitate more imaging methods for in-situ testing.

In this paper, we present a new method to study the interfacial shear stress transfer of single Si nanowires on top of a stretchable substrate (e.g. PDMS) that is subjected to uniaxial tensile loading. The nanowires are parallel to the loading direction. In-situ AFM imaging is used to record the nanowire deformation. The average axial strain in the nanowire is obtained using digital image correlation (DIC) as a function of the applied strain to the PDMS substrate. Nonlinear and bilinear cohesive shear-lag models are used to delineate the interfacial shear stress transfer characteristics for as-prepared PDMS and UVO-treated PDMS for 45 min, respectively. Three-dimensional (3D) finite element analysis (FEA) is carried out, which validates the accuracy of the analytical modeling. The interface parameters such as interfacial stiffness, shear strength, and/or fracture toughness are identified by fitting the experimentally obtained average strain in the nanowire. In addition, a parametric study with different nanowire lengths and diameters is carried out to predict the strain distribution in the nanowire, which can provide a guide to experimental design of elastic strain engineering and fracture of Si nanowires.

## 2. Experiments

In this work, Si nanowires were synthesized by chemical vapor deposition using gold nanoclusters as the catalyst and silane ( $\text{SiH}_4$ ) as the vapor-phase reactant, following the protocol reported previously (Zhu et al., 2009b). PDMS substrates were prepared using Sylgard 184 (Dow Corning) by mixing the “base” and the “curing agent” with a ratio of 10:1. Two types of PDMS substrates were used – as-prepared PDMS and UVO-treated PDMS (45 min treatment) – to investigate the effect of different bonding mechanisms on the interfacial shear stress transfer. More details of fabricating and UVO treating PDMS can be found elsewhere (Durham and Zhu, 2013; Qin and Zhu, 2011). Si nanowires were dry transferred to the PDMS substrate using the contact printing method; the contact printing method can effectively align the nanowires along a particular direction (in this case the loading direction to the PDMS substrate) (Xu et al., 2011a). Low-density Si nanowires were transferred, such that a single nanowire can be selected for the subsequent interfacial shear stress transfer study.

A miniaturized mechanical testing stage (Ernest F. Fullam) was used to apply uniaxial tensile loading to the PDMS substrate. At each desired strain, AFM was used to scan the Si nanowire while the tensile loading was paused. By analyzing the sequence of AFM images using DIC (Bruck et al., 1989; Chasiotis and Knauss, 2002), the nanowire elongation and hence average axial strain can be obtained at each strain applied to the PDMS substrate. An open-source DIC code based on Matlab was used in this work (Eberl et al., 2006), with the accuracy reported to be about 10% of a pixel. Considering that the pixel size of the AFM images is about 20 nm, an accuracy of 2 nm can be obtained. In general DIC can be used for full-field measurement, e.g. deformation and strain distribution along the nanowire in this case, which however would require features or patterns on the nanowire. This was not feasible due to the tiny size of the nanowire.

Hence the strain distribution along the nanowire was not obtained. Nevertheless it was straightforward to obtain the nanowire elongation and average strain.

Raman spectroscopy is an effective tool for noncontact measurement of strain distribution in a broad range of nanostructures such as graphene (Jiang et al., 2014; Na et al., 2016). However, many materials are not Raman sensitive; in addition, the laser spot might heat up the nanostructure locally and complicate the strain measurement if the nanostructure/substrate do not dissipate the heat efficiently, like in our case (i.e. a Si nanowire on top of an elastomeric substrate, PDMS). Therefore, other methods such as AFM are sought for the strain measurement.

### 3. Modeling

#### 3.1 Basic shear-lag formulation

Due to symmetry of the problem, only half of the nanowire/substrate system in the positive horizontal ( $x$ ) direction is considered. The nanowire has a half-length  $L$  in the  $x$ -direction with  $x = 0$  at the center of the nanowire. The constitutive equation of the nanowire can be given as  $\sigma = E_{NW}\varepsilon$ , where  $\sigma$  and  $\varepsilon$  denote the axial stress and strain in the nanowire, respectively, and  $E_{NW}$  denotes the Young's modulus of the nanowire.

Si nanowires have approximately hexagonal cross sections. The contact width between Si nanowire and PDMS was estimated (She et al., 1998) as the side length of the hexagonal cross section of the Si nanowire (Zhu et al., 2009b). The indentation depth into the PDMS due to the adhesion between Si nanowire and PDMS was found to be negligible. Hence, the equilibrium condition for the Si nanowire in the  $x$ -direction leads to

$$\frac{d\sigma}{dx} = -\frac{\tau}{h} \quad (1)$$

where  $\tau$  is the interfacial shear stress and  $h$  is the effective height, defined as the ratio between the cross-sectional area and the side length of the cross section. For a hexagonal cross section

(e.g. Si nanowire),  $h = \frac{3\sqrt{3}}{2}a$  with  $a$  as the side length. For equilateral triangular, square and pentagonal cross sections,  $h$  would be  $\frac{\sqrt{3}}{4}a$ ,  $a$ , and  $\frac{1}{4}\sqrt{5(5+2\sqrt{5})}a$ , respectively.

The relative displacement at the interface can be expressed as

$$\delta = u_m - u \quad (2)$$

where  $u_m = \varepsilon_m x$  and  $u = \varepsilon x$  represent the displacement of substrate and nanowire, respectively, with  $\varepsilon_m$  and  $\varepsilon$  the strain applied to the substrate and the axial strain of the nanowire. Both the substrate and the nanowire are assumed to be isotropic, linear elastic.

The relation between shear stress and sliding displacement can be obtained by combining Eqs. (1) and (2)

$$\tau = E_{NW} h \frac{d^2 \delta}{dx^2} \quad (3)$$

In classical shear-lag analysis,  $\tau$  is assumed to be proportional to  $\delta$ , i.e.  $\tau = K_0 \delta$ , where  $K_0$  is a stiffness constant. Eq. (3) yields the following ordinary differential equation

$$\frac{d^2 \delta}{dx^2} = \frac{K_0}{E_{NW} h} \delta \quad (4)$$

Applying the boundary conditions  $\delta = 0$  at  $x = 0$  and  $\varepsilon = 0$  at  $x = L$ , Eq. (4) can be solved. The relative displacement, the axial strain in the nanowire and the interfacial shear stress can be obtained as, respectively,

$$\delta(x) = \frac{\varepsilon_m \sinh(\beta x)}{\beta \cosh(\beta L)} \quad (5a)$$

$$\varepsilon(x) = \varepsilon_m \left(1 - \frac{\cosh(\beta x)}{\cosh(\beta L)}\right) \quad (5b)$$

$$\tau(x) = \frac{K_0 \varepsilon_m \sinh(\beta x)}{\beta \cosh(\beta L)} \quad (5c)$$

where  $\beta = \sqrt{\frac{K_0}{E_{NW} h}}$  is the shear-lag parameter (Chen et al., 2009; Cox, 1952; Nairn, 1997).

### 3.2 Integrated shear-lag models

In order to model the effects of different bonding mechanisms, such as van der Waals (vdW) interactions and chemical bonding, on the interfacial shear stress transfer, the linear interfacial behavior ( $\tau - \delta$  relationship) in the classical shear-lag analysis must be modified. Prior to sliding/damage, the classical shear-lag analysis, i.e. Eq. (5), holds. Beyond that, a number of different interface laws have been developed. Two of them, so-called nonlinear shear-lag and bilinear cohesive shear-lag models, will be discussed below.

#### 3.2.1 Nonlinear shear-lag model

In this case, the traction-separation law used is shown in Fig. 2a, with two independent interface parameters, interfacial stiffness  $K_0$  and shear strength  $\tau_c$ . When uniaxial tension is applied to the substrate, the nanowire first deforms concurrently with the substrate due to the interfacial shear stress transfer (i.e. the nanowire is bonded to the substrate). Interface sliding between the nanowire and substrate occurs when the maximum interfacial shear stress (at  $x = L$ ) reaches the shear strength  $\tau_c$  (corresponding to the relative displacement  $\delta_1$ ). Based on Eq. (5), the critical substrate strain for onset of sliding is thus given by

$$\varepsilon_{c1} = \frac{\tau_c}{\beta E_{NW} h} \coth(\beta L) = \delta_1 \beta \coth(\beta L) \quad (6)$$

When  $\varepsilon_m > \varepsilon_{c1}$ , the interface consists of two zones: a bonded zone around the center and a sliding zone emerging from the edge (two sliding zones at both edges if considering the full nanowire length), as shown schematically in Fig. 2b. In the bonded zone, with length  $L_1$  as shown in Fig. 2a, Eq. (4) holds. At the point of  $x = L_1$ , the relative displacement is exactly equal to  $\delta_1$ . With this boundary condition, the relative displacement, axial strain in the nanowire, and interfacial shear stress in the bonded zone can be solved as, respectively,

$$\delta(x) = \frac{\sinh(\beta x)}{\sinh(\beta L_1)} \delta_1 \quad (7a)$$

$$\varepsilon(x) = \varepsilon_m - \delta_1 \beta \frac{\cosh(\beta x)}{\sinh(\beta L_1)} \quad (7b)$$

$$\tau(x) = \frac{\sinh(\beta x)}{\sinh(\beta L_1)} \tau_c \quad (7c)$$

In the sliding zone, the relative displacement exceeds  $\delta_1$ . The interfacial shear stress remains constant ( $\tau = \tau_c$ ), substituting which into Eq. (3) leads to

$$\frac{d^2 \delta}{dx^2} = \frac{\tau_c}{E_{NW} h} \quad (8)$$

Applying the boundary conditions  $\delta(L_1) = \delta_1$  and  $\varepsilon = 0$  at  $x = L$ , the relative displacement and axial strain in the nanowire be solved as, respectively,

$$\delta(x) = \frac{\beta^2}{2} \delta_1 (x + L_1 - 2L)(x - L_1) + \varepsilon_m (x - L_1) + \delta_1 \quad (9a)$$

$$\varepsilon(x) = \frac{\tau_c}{E_{NW} h} (L - x) = \beta^2 \delta_1 (L - x) \quad (9b)$$

Often times the axial strain at the center of the nanostructures (e.g. graphene) is measured using tools like Raman spectroscopy, which can be used to study interfacial stress transfer (Jiang et al., 2014). In this case, the axial strain at the center of the nanowire is

$$\varepsilon(0) = \varepsilon_m - \delta_1 \beta \frac{1}{\sinh(\beta L_1)} = \varepsilon_m - \frac{\tau_c}{\beta E_{NW} h \sinh(\beta L_1)} \quad (10)$$

$L_1$  can be obtained by requiring the axial strain in the nanowire to be continuous at  $x = L_1$

$$\coth(\beta L_1) + \beta(L - L_1) = \frac{\beta E_{NW} h \varepsilon_m}{\tau_c} \quad (11)$$

Once  $L_1$  is known, the relative displacement, axial strain in the nanowire, and interfacial shear stress in the entire nanowire can all be calculated from Eqs. (7) and (9), as shown in Figs. 3a-c, respectively. As the sliding zone develops from the edge and approaches the center, the center strain in the nanowire eventually saturates at a plateau strain

$$\varepsilon_p = \frac{\tau_c}{E_{NW} h} L \quad (12)$$

The average strain along the nanowire is given by

$$\bar{\varepsilon} = \frac{1}{L} \int_0^L \varepsilon(x) dx = \frac{1}{L} \left[ \int_0^{L_1} \left( \varepsilon_m - \delta_1 \beta \frac{\cosh(\beta x)}{\sinh(\beta L_1)} \right) dx + \int_{L_1}^L \left( \frac{\tau_c}{E_{NW} h} (L - x) \right) dx \right]$$

$$= \frac{\varepsilon_m L_1}{L} + \frac{(\beta^2 (L - L_1)^2 / 2 - 1) \tau_c}{\beta^2 L E_{NW} h} \text{ when } L_1 > 0 \quad (13a)$$

$$= \frac{\tau_c}{2 E_{NW} h} L \text{ when } L_1 = 0 \quad (13b)$$

$L_1$  is a function of  $\varepsilon_m$  according to Eq. (11). When  $L_1 > 0$ , the average strain along the nanowire is a function of  $K_0$  and  $\tau_c$  in addition to  $\varepsilon_m$ . When  $L_1 = 0$  (attainable only when  $\varepsilon_m$  is much larger than  $\varepsilon_{c1}$ ), the average strain is only a function of  $\tau_c$ , irrespective of  $\varepsilon_m$ . Fig. 3d plots the axial strain at the center of the nanowire  $\varepsilon(0)$  and the average strain  $\bar{\varepsilon}$  as functions of the strain applied to the substrate  $\varepsilon_m$ .

### 3.2.2 Bilinear cohesive shear-lag model

Cohesive zone models have widely been used in the continuum study of interface debonding and sliding (Needleman, 1990; Park and Paulino, 2013). In spite of some experimental studies of microscale cohesive laws (Li et al., 2005; Zhu et al., 2009a), the existing cohesive models are typically phenomenological because it is difficult to directly measure the cohesive laws for interfaces. Recently some nanoscale cohesive laws have been derived from atomistic simulations (Jiang et al., 2006; Liu and Xu, 2014; Meng et al., 2017).

Cohesive laws can assume a variety of forms. In this work, a simple bilinear traction-separation law is used, as shown in Fig. 2c, with three independent interface parameters, interfacial stiffness  $K_0$ , shear strength  $\tau_c$ , and mode II fracture toughness  $G$ . In this model, it is assumed that the interfacial shear stress, after the initial linear increase, decreases linearly till vanishing. With the increasing strain applied to the substrate, the nanowire-substrate interface may gradually develop into three zones: a bonded zone around the center ( $0 < x < L_1$ ), a damaged zone ( $L_1 < x < L_2$ ), and a debonded zone ( $L_2 < x < L$ ) (Guo and Zhu, 2015), as

shown schematically in Fig. 2d. Two critical substrate strains,  $\varepsilon_{c1}$  and  $\varepsilon_{c2}$ , correspond to the onset of the damage and the debonding, respectively.

The first critical substrate strain  $\varepsilon_{c1}$  is also given by Eq. (6). In the bonded zone, the relative displacement, axial strain in the nanowire, and interfacial shear stress are given by Eq. (7). In the damaged zone, the interfacial shear stress is given by  $\tau = \tau_c \frac{\delta_2 - \delta}{\delta_2 - \delta_1}$ , substituting which into Eq.

(3) leads to

$$\frac{d^2\delta}{dx^2} = \alpha^2(\delta_2 - \delta) \quad (14)$$

where  $\alpha = \sqrt{\tau_c / (E_{NW} h (\delta_2 - \delta_1))}$ . Applying the boundary condition  $\delta = \delta_1$  and the continuity condition of the axial strain in the nanowire at  $x = L_1$ , the relative displacement, axial strain in the nanowire, and interfacial shear stress can be solved as, respectively,

$$\delta(x) = A \cos(\alpha(x - L_1)) + B \sin(\alpha(x - L_1)) + \delta_2 \quad (15a)$$

$$\varepsilon(x) = \varepsilon_m + A \alpha \sin(\alpha(x - L_1)) - B \alpha \cos(\alpha(x - L_1)) \quad (15b)$$

$$\tau(x) = -\frac{\tau_c}{\delta_2 - \delta_1} \left( A \cos(\alpha(x - L_1)) + B \sin(\alpha(x - L_1)) \right) \quad (15c)$$

where  $A = \delta_2 - \delta_1$  and  $B = \delta_1 \beta \coth(\beta L_1) / \alpha$ .  $L_1$  can be determined by applying boundary condition  $\varepsilon = 0$  at  $x = L$ , given as

$$-\varepsilon_m = A \alpha \sin(\alpha(L - L_1)) - B \alpha \cos(\alpha(L - L_1)) \quad (16)$$

Once  $L_1$  is known, the relative displacement, axial strain in the nanowire, and interfacial shear stress in the entire nanowire can be calculated from Eqs. (7) and (15), as shown in Figs. 4a-c, respectively.

At the second critical substrate strain  $\varepsilon_{c2}$ , the relative displacement at the edge of the nanowire reaches  $\delta_2$ . Eq. (15a) becomes

$$A \cos(\alpha(L - L_1)) + B \sin(\alpha(L - L_1)) = 0 \quad (17)$$

This equation gives a critical value of  $L_1$ , after which the corresponding strain applied to the substrate,  $\varepsilon_{c2}$ , can be determined by Eq. (16).

When  $\varepsilon_m > \varepsilon_{c2}$ , the interface consists of three zones: a bonded zone, a damaged zone, and a debonded zone. The bonded zone and the damaged zone have total length of  $L_2$  as shown in Fig. 2d. The relative displacement, axial strain in the nanowire, and interfacial shear stress in the bonded zone and the damaged zone still take the same form of Eqs. (7) and (15), respectively. In the debonded part, the interfacial shear stress and axial strain in the nanowire become zero. For completeness, Eq. (3) simply becomes

$$\frac{d^2\delta}{dx^2} = 0 \quad (18)$$

Applying the boundary condition  $\delta = \delta_2$  at  $x = L_2$  and the axial strain in the nanowire is zero in the zone, the relative displacement can be solved as

$$\delta(x) = \varepsilon_m(x - L_2) + \delta_2 \quad (19)$$

The length of  $L_1$  and  $L_2$  can be obtained simply by solving Eqs. (16) and (17) simultaneously by substituting  $L$  with  $L_2$ . The axial strain at the center of the nanowire is also given by Eq. (10) after  $L_1$  is solved. The average strain in the nanowire is given by

$$\begin{aligned} \bar{\varepsilon} &= \frac{1}{L} \int_0^L \varepsilon(x) dx = \frac{1}{L} \left[ \int_0^{L_1} \left( \varepsilon_m - \delta_i \beta \frac{\cosh(\beta x)}{\sinh(\beta L_1)} \right) dx + \int_{L_1}^{L_2} \left( \varepsilon_m + A \sin(\alpha(x - L_1)) - \right. \right. \\ &\quad \left. \left. B \alpha \cos(\alpha(x - L_1)) \right) dx + \int_{L_2}^L (0) dx \right] \\ &= \frac{\varepsilon_m L_2 - \delta_i}{L} + \frac{A(1 - \cos(\alpha(L_2 - L_1))) - B \sin(\alpha(L_2 - L_1))}{L} \text{ when } L_1 > 0 \end{aligned} \quad (20a)$$

$$= \frac{\varepsilon_m L_2}{L} + \frac{A(1 - \cos(\alpha L_2)) - B \sin(\alpha L_2)}{L} \text{ when } L_1 = 0 \text{ and } L_2 > 0 \quad (20b)$$

$$= 0 \text{ when } L_2 = 0 \quad (20c)$$

Fig. 4d plots the axial strain at the center of the nanowire  $\varepsilon(0)$  and the average strain  $\bar{\varepsilon}$  as functions of the strain applied to the substrate  $\varepsilon_m$ .

### 3.3 Finite element modeling

In addition to the analytical modeling, FEA (ABAQUS, version 6.14) was employed to evaluate the assumptions in the analytical modeling and to compare with experimental results. The FEA models in accordance with both the nonlinear and cohesive shear-lag models were developed. Again only half of the nanowire/PDMS system was considered by taking advantage of the symmetry of the problem in the horizontal direction.

In a 3D model, C3D8R reduced linear brick element was used to model Si nanowire and PDMS. Both materials are considered isotropic, linearly elastic with the following properties: Young's modulus 120 GPa and 2 MPa and Poisson's ratio 0.3 and 0.48, for Si nanowire and PDMS, respectively. Note that Young's modulus of Si nanowires was reported to exhibit size effect (Zhu et al., 2009b). For the diameter of 20 nm, the Young's modulus of Si nanowires is about 120 GPa. For UVO-treated PDMS, a thin layer on the surface is converted into a stiff "skin" layer. A Young's modulus of 80 MPa (Efimenko et al., 2005) was used for a surface layer (5 nm in thickness) in the FEA simulations. The interface between Si nanowire and PDMS was modeled using a surface-based cohesive contact approach. Similar to modeling of cohesive elements, a traction-separation law is used to describe the constitutive behavior of the interface. For the cohesive shear-lag model, the traction-separation law is readily available in ABAQUS. For the nonlinear shear-lag model, the built-in bilinear traction-separation law in ABAQUS was modified with a very large fracture toughness  $G$ . Both cohesive laws were similarly implemented as cohesive contact properties using a surface-to-surface discretization method. Only mode II parameters were considered while mode I parameters were kept relatively high to prohibit normal direction penetration in compression and separation in tension.

The normal strains along the nanowire predicted by the analytical model and the 3D FEA model using the brick elements are shown in Fig. 5 for the purpose of comparison. Note that for the FEA model, the plotted normal strain is at the centroid of the cross section. It can be seen that for small nanowire diameter (e.g. 10 nm), the analytical model agrees well with the FEA model. The discrepancy increases with the nanowire diameter. For example, the discrepancy for the strain at the center of the nanowire is 0.9%, 2.1%, 6.4%, 15.8%, and 38.9% for the radius of 10, 50, 100, 200, and 400 nm, respectively, for the nanowire length of 22.4  $\mu\text{m}$ , the as-prepared PDMS, and the applied substrate strain of 18%. The FEA model further shows that for small nanowire diameter, the normal strain distribution is nearly uniform at the nanowire cross section, i.e. the bending contribution is negligible. But with increasing nanowire diameter, the bending contribution becomes more pronounced, which explains the increasing discrepancy mentioned above. It should be noted that the shear-lag model considers only the axial loading along the nanowire and neglect bending. For a typical nanowire the radius is less than 50 nm, therefore the shear-lag model provides a close approximation.

1D beam element was commonly used in modeling the interface behavior of a wire-shaped structure embedded in a matrix (Su et al., 2014; Zhao et al., 2016). In the model using the 3D brick element, the contact area between the nanowire and substrate is one flat side surface of the nanowire (note that Si nanowire has a hexagonal cross section). Using the beam element, however, the contact area is half of the entire side surface area, which leads to overestimation of the interfacial shear stress transfer for a wire on top of a substrate.

Strictly speaking, Si is anisotropic (Hopcroft et al., 2010) and PDMS exhibits hyperelastic behavior. FEA simulations were conducted using both isotropic and anisotropic constitutive laws for Si nanowire. The results showed no noticeable difference between the two simulations. The

large length-to-diameter ratio of the Si nanowire justifies the isotropic approximation. A common hyperelastic model, e.g. Mooney-Rivlin model, was tested against the linear elastic model. The results showed that for the range of strain applied to PDMS during the experiments (below 25%), both models yielded nearly the same results. This is expected as PDMS shows a nearly linear elastic response below 30% strain (Johnston et al., 2014).

#### 4. Comparison between experiments and modeling

For the nonlinear shear-lag model, two features can be observed regarding the relationship between the average strain in the nanowire  $\bar{\epsilon}$  and the strain applied to the substrate  $\epsilon_m$ . Prior to sliding, the axial strain in the nanowire  $\epsilon(x)$  is proportional to  $\epsilon_m$  according to Eq. (5b). So the first feature is that when  $\epsilon_m$  is relatively small,  $\bar{\epsilon}$  is proportional to  $\epsilon_m$  with the proportional factor of  $\frac{1}{L} \int_0^L \left(1 - \frac{\cosh(\beta x)}{\cosh(\beta L)}\right) dx = 1 - \frac{\sinh(\beta L)}{\beta L \cosh(\beta L)}$ , which is the initial slope of the curve in Fig. 3d. Since  $\beta$  is a sole function of the stiffness  $K_0$  (Young's modulus and effective height of the nanowire are known), the initial slope can be used to determine  $K_0$ . The second feature is that when  $\epsilon_m$  is much larger than the critical strain for onset of sliding  $\epsilon_{c1}$ ,  $\bar{\epsilon}$  reaches its plateau value, which is a sole function of the interfacial shear strength  $\tau_c$ , irrespective of  $\epsilon_m$ . Therefore, the plateau average strain can be used to determine  $\tau_c$ .

For the case of as-prepared PDMS, AFM images of the Si nanowire at five different strains applied to the substrate (from 0 to 20.4%) were obtained. The nanowire was 22.4  $\mu\text{m}$  in length. The corresponding average strains in the nanowire were calculated using DIC, as shown in Fig. 6a. As the DIC resolution is 2 nm, the error in the average strain in the nanowire was estimated to be  $\pm 0.01\%$ . It can be seen that the average strain in the nanowire approaches a constant value with the increasing substrate strain, following well the second feature in the nonlinear shear-lag analysis. By fitting Eq. (13b) to the experimental data, more specifically, the last data point, the

interfacial shear strength  $\tau_c$  was obtained as 0.77 MPa. Then, the stiffness  $K_0$  value of 2.15 TPa/m was determined by fitting to the rest of the data points. There were relatively few data points available due to the small strains involved in this experiment, so the initial slope was not well defined. Hence the first feature was not used to fit the cohesive parameters.

For the bilinear shear-lag model, the first feature in the nonlinear shear-lag model – at a relatively small  $\varepsilon_m$ ,  $\bar{\varepsilon}$  is proportional to  $\varepsilon_m$  (with the same proportional factor) – holds true.  $\bar{\varepsilon}$  increases with increasing  $\varepsilon_m$  until reaching a peak value, after which it decreases with increasing  $\varepsilon_m$  due to the development of the debonded zone. As shown in Fig. 4d, the peak value of  $\bar{\varepsilon}$  occurs between the two critical substrate strains,  $\varepsilon_{c1}$  and  $\varepsilon_{c2}$ .

For the case of UVO-treated PDMS, AFM images of the Si nanowire at six different strains applied to the substrate (from 0 to 23.5%) were obtained. The nanowire was 16.4  $\mu\text{m}$  in length. The corresponding average strains in the nanowire are shown in Fig. 6b. It can be seen that the average strain in the nanowire increases with the substrate strain, reaches a peak value and decreases, following the general trend predicted by the cohesive shear-lag model. By fitting the initial slope to  $1 - \frac{\sinh(\beta L)}{\beta L \cosh(\beta L)}$ ,  $\beta$  and then  $K_0$  was obtained as 39.9 TPa/m. Due to the rather complicated relationship between  $\bar{\varepsilon}$  and  $\varepsilon_m$ , it is deemed not feasible to determine  $\tau_c$  and  $G$  one at a time by fitting. Rather  $\tau_c$  and  $G$  can be determined together. To provide benchmark values for fitting  $\tau_c$  and  $G$ , the  $\tau_c$  value obtained from the method of “the most-bent state” (Qin and Zhu, 2011) and  $\tau_c^2/K_0$  were used, respectively. In this case,  $\tau_c$  and  $G$  were determined to be 16.8 MPa and 8.1 J/m<sup>2</sup>, respectively.

## 5. Discussion

### 5.1 Shear-lag models for vdW interactions and chemical bonding

The two models discussed above have some distinctive features, e.g. a plateau strain for the nonlinear shear-lag model and a peak-then-decreasing strain for the bilinear shear-lag model. These features determine that it is sufficient and necessary to fit the experimental data of the as-prepared and UVO-treated PDMS with the nonlinear shear-lag and bilinear shear-lag models, respectively, as supported by the fitting results shown in Fig. 6.

In the case of Si nanowire on as-prepared PDMS, the bonding is based on vdW interactions, which is relatively weak. There are two kinds of vdW forces: weak London dispersion forces that form between instantaneously induced dipoles and stronger dipole-dipole forces (Israelachvili, 2011). Due to the ubiquitous nature of vdW interactions, the bonds can re-form after breaking under deformation, which is captured by a constant interfacial shear strength  $\tau_c$  in the nonlinear shear-lag model. Re-formation of the vdW interactions between Si and as-prepared PDMS after breaking is experimentally confirmed by repeatedly measuring the adhesion between them, as shown in Fig. A.1(a).

The nonlinear shear-lag model has been used to delineate the interfacial shear stress transfer at graphene/polymer interfaces with vdW interactions (Jiang et al., 2014; Wang et al., 2016), graphene oxide/polymer interfaces with hydrogen bonding (Dai et al., 2016), and cellulose nanofibril interfaces with hydrogen bonding (Meng et al., 2017). In all these cases, a constant shear strength is present under large relative displacement across the interface. Note that Jiang et al. derived the cohesive law for CNT/polymer interface directly from the vdW force (Jiang et al., 2006). The authors found that for an infinite polymer matrix, the interfacial shear stress vanishes; the shear stress becomes non-zero only for a finite polymer matrix. However, they did not consider re-formation of the vdW interaction. By contrast, considering re-formation of the hydrogen bonds, a constant shear strength was obtained (Meng et al., 2017).

When PDMS is UVO-treated, covalent bonds, i.e. siloxane bonds (-Si-O-Si-), are formed through condensation reaction between Si nanowire and PDMS (Sun and Rogers, 2007). These covalent bonds are known to be stronger than vdW interactions, which is consistent with the larger  $\tau_c$  in the case of UVO-treated PDMS. An activation energy barrier must be overcome in order for the condensation reaction to take place. The reaction rate is temperature dependent. The bonds may not be able to re-form fast enough after breaking at the experimental loading rate and temperature, which is confirmed by repeatedly measuring the adhesion between Si and UVO-treated PDMS (Fig. A.1(b)). This feature of bond breaking is captured by the damage and debonded zones in the bilinear cohesive shear-lag model.

Molecular dynamics (MD) simulations have been recently used to obtain the traction-separation relations at nanoscale interfaces. A traction-separation law in shear mode extracted from the MD simulations has been implemented in a continuum model accounting for debonding in graphite nanoplatelet polymer composites (Safaei et al., 2015). (Li and Seidel, 2015) obtained a shear traction-separation law for covalent bonds between graphene and polyethylene, which exhibited softening and damage at large deformation. (Liu and Xu, 2014) simulated the response of covalent bonds between graphene oxide and glutaraldehyde. The traction-separation law obtained from the MD simulations showed damage and debonding as the chemical bonds failed. The atomistically derived traction-separation curves associated with chemical bonding all show damage and debonding after the initial stiffening. Typically these curves can be sophisticated. But it is known that the cohesive strength and fracture toughness are the key parameters to describe a fracture process while the detailed form of the traction-separation curve is less important. Therefore, it is reasonable to use the simple bilinear traction-separation law to model the Si nanowire/PDMS interface with chemical bonding.

## 5.2 Effect of UVO treatment

Table 1 lists the best fitting values for the cohesive parameters for both the nonlinear and bilinear shear-lag models. The interfacial stiffness  $K_0$  for the case of UVO-treated PDMS is higher than that of as-prepared PDMS.  $K_0$  is a measure of the effective stiffness of the substrate. The UVO-treated PDMS has a stiffer surface layer (Efimenko et al., 2005), which is expected to lead to larger  $K_0$ .  $\beta L$  describes the efficacy of shear stress transfer across the interface.  $\beta L$  is equal to 0.29 and 0.93, respectively, for the as-prepared and UVO-treated PDMS, which indicates that the shear stress transfer is more effective in the UVO-treated case. The interfacial shear strength for the case of UVO-treated PDMS is also higher than that of as-prepared PDMS, which can be attributed to the stronger nature of chemical bonds between Si nanowire and UVO-treated PDMS. Using “the most-bent state” method, Qin and Zhu found that in the case of Si nanowires on PDMS, the shear strength starts at 0.3 MPa without UVO treatment and increases rapidly up to 9.4 MPa at 45 min of treatment (and 10.6 MPa at 60 min of treatment) (Qin and Zhu, 2011). The present results are in accordance with the previous ones in terms of the rapid increase in shear strength as a result of UVO treatment, but are consistently larger. As mentioned earlier, the most-bent state method can lead to large errors. In particular, the smoothing in the data analysis can underestimate the results. It should be noted that while chemical bonds due to the UVO treatment lead to higher interfacial stiffness and shear strength, they are difficult to reform after breaking, limiting the interfacial stress transfer.

## 5.3 Effects of interface parameters

The interface parameters were varied in order to evaluate their effect on the central and average strains of Si nanowire on top of as-prepared and UVO-treated PDMS. The Si nanowire dimensions used for both cases were the same as in the experiments. First, the effect of the

interfacial stiffness  $K_0$  was studied. For the case of as-prepared PDMS, the shear strength was kept constant ( $\tau_c = 0.8$  MPa) while  $K_0$  was varied from 1.1 to 4.3 TPa/m. Fig. 7a shows that the central and average strains increase with increasing  $K_0$  as this parameter controls the slope of the initial linear part of the plot. However, the first critical strain  $\varepsilon_{c1}$  decreases with increasing  $K_0$ , which indicates earlier damage initiation at both edges of Si nanowire. For the case of UVO-treated PDMS, both the shear strength ( $\tau_c = 16.8$  MPa) and the fracture toughness ( $G_c = 8.1$  N/m) were kept constant while  $K_0$  was varied from 19.9 to 79.8 TPa/m. The same trend was observed in Fig. 8a regarding the central and average strains when it comes to increasing  $K_0$ , namely increase of both strains and earlier onset of damage due to decreasing  $\varepsilon_{c1}$ . However, the second critical strain  $\varepsilon_{c2}$  is nearly unchanged.

Next, the interface shear strength  $\tau_c$  was varied. At this time, for the case of as-prepared PDMS, the interfacial stiffness was kept constant ( $K_0 = 2.1$  TPa/m) while  $\tau_c$  ranged from 0.4 to 1.5 MPa. It can be seen from Fig. 7b that while the shear strength does not have much effect at lower  $\varepsilon_m$  (e.g., 2%), larger central and average strain ensue with increasing shear strength at larger  $\varepsilon_m$ . In addition, larger shear strength results in larger first critical strain  $\varepsilon_{c1}$ , which means that the interface can undergo a larger  $\varepsilon_m$  before damage initiates. For the case of UVO-treated PDMS, both interfacial stiffness ( $K_0 = 39.9$  TPa/m) and fracture toughness ( $G_c = 8.1$  N/m) were kept constant while  $\tau_c$  was varied from 8.4 to 25.4 MPa. As shown in Fig. 8b, with increasing shear strength the first critical strain  $\varepsilon_{c1}$  decreases, the same as the case of as-prepared PDMS, but the second critical strain  $\varepsilon_{c2}$  decreases. Note that due to the given interfacial stiffness and fracture toughness, a maximum shear strength of 25.4 MPa is defined, in which case there is no damage before debonding as shown in Fig. 2d (i.e.  $\delta_1 = \delta_2$ ).

Finally, the interface fracture toughness  $G_c$  was varied only for the case of UVO-treated PDMS. Both the interfacial stiffness ( $K_0 = 39.9$  TPa/m) and the shear strength ( $\tau_c = 16.8$  MPa) were kept constant while  $G_c$  ranged from 4.0 to 16.2 N/m. In contrast to  $K_0$  and  $\tau_c$  that affect strain distribution in both the fully bonded part and damaged part,  $G_c$  only comes into play after damage initiates. The effect of  $G_c$  on the central and average strains is shown in Fig. 8c. It can be seen that the first critical strain  $\varepsilon_{c1}$  does not depend on  $G_c$ , but the second critical strain  $\varepsilon_{c2}$  increases with increasing  $G_c$ , which delays debonding at the interface. This is consistent with the less pronounced softening of the central and average strains for higher  $G_c$ .

#### 5.4 Implication for elastic strain engineering and fracture of nanowires

An additional parametric study was carried out to investigate the effect of nanowire dimensions (length and diameter) with implication for elastic strain engineering and fracture of Si nanowires. Here the traction-separation laws shown in Figure 2 with the interface parameters in Tables 1 and 2 were used for the as-prepared and UVO-treated PDMS.

For the case of as-prepared PDMS, the radius of 10 nm was kept constant with the length varying between 22.4 and 112  $\mu\text{m}$  and then the length of 22.4  $\mu\text{m}$  was kept constant with the radius varying between 2 and 10 nm. Figs. 9a and b show the strain distribution along the Si nanowire length and the maximum strain for a range of  $\varepsilon_m$  up to 21%, respectively. It can be seen that the longer or the thinner the Si nanowire, the higher the Si nanowire strain, which characterizes a more efficient interfacial stress transfer (assuming the interfacial properties unchanged). This is understandable as  $\beta L$  characterizes the efficacy of shear stress transfer across the interface. Elastic strain engineering has received much interest recently. Straining a nanostructure on top of a stretchable substrate via interfacial shear transfer is a commonly used method. It is critical to know precisely the local strain, which is generally difficult to measure.

Interfacial mechanics modeling with measured traction-separation relationship, as conducted here as an example, can predict the local strain. Methods like Raman spectroscopy have been used to measure local strain, but the Grüneisen parameter (i.e. characterizing relationship between strain and Raman shift) must be obtained first, which would depend on the strain measurement. In addition, like the fragmentation test, it might be possible to measure the fracture strain of the nanowires using this method. As shown in Figs. 9c and d, for the case of as-prepared PDMS the maximum strains are relatively small for the given ranges of nanowire length and diameter, when compared to the reported fracture strains of Si nanowires (Zhu et al., 2009b). This is expected for the case of as-prepared PDMS since the bonding is relatively weak.

Similarly, for the case of UVO-treated PDMS, the radius of 10 nm was kept constant with the length varying between 16.4 and 82  $\mu\text{m}$  and then the length of 16.4  $\mu\text{m}$  was kept constant with the radius varying between 2 and 10 nm. Figs. 10a and b show the strain distribution along the Si nanowire and the maximum strain for a range of  $\varepsilon_m$  up to 24%, respectively. The effect of nanowire length and radius is the same as that for the case of as-prepared PDMS. However, because the stress transfer is relatively more effective in this case, the strain in the nanowire becomes much larger, potentially reaching the fracture strain of Si nanowires. (Zhu et al., 2009b) reported that the fracture strain of Si nanowires with 10 nm radius is about 6-7%. Fig. 10c shows that for a 82  $\mu\text{m}$  long Si nanowire, the maximum strain is nearly 7% when  $\varepsilon_m$  is 7%, which can lead to the nanowire fracture. The same holds true for a Si nanowire with 2 nm radius, as shown in Fig. 10d.

## 6. Conclusions

We have reported a new method to study the interfacial shear stress transfer of single nanowires on top of a stretchable substrate. In-situ AFM testing was carried out to measure the

average axial strain in the nanowire as a function of the applied strain to the PDMS substrate. Two types of substrates, as-prepared and UVO-treated PDMS, were selected to examine the effect of vdW interactions and chemical bonding on the interfacial shear stress transfer. It was found that nonlinear and bilinear cohesive shear-lag models can work well for the cases of vdW interactions and chemical bonding, respectively. The accuracy of the shear-lag models was validated by 3D FEA. The interface parameters such as interfacial stiffness, shear strength, and/or fracture toughness were identified by fitting the experimentally obtained average strain in the nanowire. A constant interfacial shear strength was found due to the breaking and re-formation of vdW interactions. UVO treatment induced chemical bonding led to much increased interfacial stiffness and shear strength, but the chemical bonds were difficult to re-form, leading to debonding of the interface. A parametric study was carried out to evaluate the effect of the interfacial stiffness, shear strength and fracture toughness on the nanowire center and average strains. An additional parametric study with different nanowire lengths and diameters was used to predict the strain distribution in the nanowire, which can provide a guide to experimental design of elastic strain engineering and fracture of Si nanowires. The method and results reported in this work can be extended to the interfaces between other 1D nanomaterials (e.g. nanotubes and nanofibers) or 2D nanomaterials and polymers.

## **Acknowledgements**

This work was supported in part by the National Science Foundation (NSF) through Award No. CMMI-1762511. The authors would like to thank F. Xu for his help in the AFM measurements.

## Appendix A. Measuring adhesion between Si and PDMS

We designed a model experiment to measure the force profiles corresponding to vdW interactions and chemical bonding. Two PDMS samples with cross-sectional area of  $1 \text{ cm}^2$  were prepared with one of them as-prepared and the other UVO treated; the sample preparation and treatment followed the same procedure used in the nanowire-PDMS interfacial mechanics study. The PDMS samples were glued to glass substrates that are mounted to a mechanical testing machine, while a silicon wafer was mounted to the other end of the testing machine. The experiment measured the pull-off (adhesion) forces between the silicon wafer and the PDMS samples at a constant rate of  $0.1 \text{ mm/s}$  after different durations of contact.

Fig. A.1(a) shows the results for the as-prepared PDMS sample. The first pull-off was measured right after the two parts made contact ( $\sim 2 \text{ sec}$ ), showing the peak force of  $0.045 \text{ N}$ . The contact and pull-off cycles were repeated several times. It can be seen that the pull-off force is independent of the contact duration. This set of tests strongly suggested that vdW interactions are spontaneous and can be re-formed after breaking.

Fig. A.1(b) shows the results for the UVO-treated PDMS sample. The first pull-off was measured after  $2 \text{ min}$  contact of the two parts (PDMS and Si wafer), showing the peak force of  $7.2 \text{ N}$ , which is much larger compared to the as-prepared sample. This indicates that chemical bonding is much stronger than vdW interactions. The contact and pull-off cycles were repeated several times. The pull-off force after the next  $2 \text{ min}$  contact was smaller than the first one, which increased after  $10 \text{ min}$  contact but was still smaller than the first one. Two conclusions were drawn from these tests: 1) some of the chemical bonds formed during the first contact did not re-form after breaking, and 2) the strength of chemical bonding was time dependent. These conclusions were supported by additional tests.

## References

- Bruck, H.A., McNeill, S.R., Sutton, M.A., Peters, W.H., 1989. Digital image correlation using Newton-Raphson method of partial differential correction. *Exp. Mech.*  
<https://doi.org/10.1007/BF02321405>
- Chasiotis, I., Knauss, W.G., 2002. A new microtensile tester for the study of MEMS materials with the aid of atomic force microscopy. *Exp. Mech.*  
<https://doi.org/10.1177/0018512002042001789>
- Chen, B., Wu, P.D., Gao, H., 2009. A characteristic length for stress transfer in the nanostructure of biological composites. *Compos. Sci. Technol.*  
<https://doi.org/10.1016/j.compscitech.2009.02.012>
- Chen, X., Zhang, L., Zheng, M., Park, C., Wang, X., Ke, C., 2015. Quantitative nanomechanical characterization of the van der Waals interfaces between carbon nanotubes and epoxy. *Carbon N. Y.* <https://doi.org/10.1016/j.carbon.2014.10.065>
- Chen, Y., Liu, Y., Yan, Y., Zhu, Y., Chen, X., 2016a. Helical coil buckling mechanism for a stiff nanowire on an elastomeric substrate. *J. Mech. Phys. Solids.*  
<https://doi.org/10.1016/j.jmps.2016.05.020>
- Chen, Y., Zhu, Y., Chen, X., Liu, Y., 2016b. Mechanism of the Transition From In-Plane Buckling to Helical Buckling for a Stiff Nanowire on an Elastomeric Substrate. *J. Appl. Mech.* <https://doi.org/10.1115/1.4032573>
- Coleman, J.N., Khan, U., Blau, W.J., Gun'ko, Y.K., 2006. Small but strong: A review of the mechanical properties of carbon nanotube-polymer composites. *Carbon N. Y.*  
<https://doi.org/10.1016/j.carbon.2006.02.038>
- Cox, H.L., 1952. The elasticity and strength of paper and other fibrous materials. *Br. J. Appl.*

- Phys. <https://doi.org/10.1088/0508-3443/3/3/302>
- Dai, Z., Wang, G., Liu, L., Hou, Y., Wei, Y., Zhang, Z., 2016. Mechanical behavior and properties of hydrogen bonded graphene/polymer nano-interfaces. *Compos. Sci. Technol.* <https://doi.org/10.1016/j.compscitech.2016.09.005>
- Ding, W., Eitan, A., Fisher, F.T., Chen, X., Dikin, D.A., Andrews, R., Brinson, L.C., Schadler, L.S., Ruoff, R.S., 2003. Direct Observation of Polymer Sheathing in Carbon Nanotube-Polycarbonate Composites. *Nano Lett.* <https://doi.org/10.1021/nl0345973>
- Drzal, L.T., Madhukar, M., 1993. Fibre-matrix adhesion and its relationship to composite mechanical properties. *J. Mater. Sci.* <https://doi.org/10.1007/BF01151234>
- Durham, J.W., Zhu, Y., 2013. Fabrication of functional nanowire devices on unconventional substrates using strain-release assembly. *ACS Appl. Mater. Interfaces.* <https://doi.org/10.1021/am302384z>
- Eberl, C., Thompson, R., Gianola, D., 2006. *Digital Image Correlation and Tracking with Matlab. Image* (Rochester, N.Y.).
- Efimenko, K., Rackaitis, M., Manias, E., Vaziri, A., Mahadevan, L., Genzer, J., 2005. Nested self-similar wrinkling patterns in skins. *Nat. Mater.* <https://doi.org/10.1038/nmat1342>
- Guo, G., Zhu, Y., 2015. Cohesive-Shear-Lag Modeling of Interfacial Stress Transfer Between a Monolayer Graphene and a Polymer Substrate. *J. Appl. Mech.* <https://doi.org/10.1115/1.4029635>
- Han, X., Kou, L., Lang, X., Xia, J., Wang, N., Qin, R., Lu, J., Xu, J., Liao, Z., Zhang, X., Shan, X., Song, X., Gao, J., Guo, W., Yu, D., 2009. Electronic and mechanical coupling in bent ZnO nanowires. *Adv. Mater.* <https://doi.org/10.1002/adma.200900956>
- Hopcroft, M.A., Nix, W.D., Kenny, T.W., 2010. What is the Young's modulus of silicon? *J.*

- Microelectromechanical Syst. <https://doi.org/10.1109/JMEMS.2009.2039697>
- Hou, L., Wang, S., Huang, H., 2015. A simple criterion for determining the static friction force between nanowires and flat substrates using the most-bent-state method. *Nanotechnology*. <https://doi.org/10.1088/0957-4484/26/16/165702>
- Israelachvili, J.N., 2011. *Intermolecular and Surface Forces: Third Edition*, Intermolecular and Surface Forces: Third Edition. <https://doi.org/10.1016/C2011-0-05119-0>
- Jiang, L.Y., Huang, Y., Jiang, H., Ravichandran, G., Gao, H., Hwang, K.C., Liu, B., 2006. A cohesive law for carbon nanotube/polymer interfaces based on the van der Waals force. *J. Mech. Phys. Solids*. <https://doi.org/10.1016/j.jmps.2006.04.009>
- Jiang, T., Huang, R., Zhu, Y., 2014. Interfacial sliding and buckling of monolayer graphene on a stretchable substrate. *Adv. Funct. Mater.* <https://doi.org/10.1002/adfm.201301999>
- Johnston, I.D., McCluskey, D.K., Tan, C.K.L., Tracey, M.C., 2014. Mechanical characterization of bulk Sylgard 184 for microfluidics and microengineering. *J. Micromechanics Microengineering*. <https://doi.org/10.1088/0960-1317/24/3/035017>
- Li, S., Thouless, M.D., Waas, A.M., Schroeder, J.A., Zavattieri, P.D., 2005. Use of mode-I cohesive-zone models to describe the fracture of an adhesively-bonded polymer-matrix composite. *Compos. Sci. Technol.* <https://doi.org/10.1016/j.compscitech.2004.07.009>
- Li, Y., Seidel, G.D., 2015. Multiscale modeling of functionalized interface effects on the effective elastic material properties of CNT-polyethylene nanocomposites. *Comput. Mater. Sci.* <https://doi.org/10.1016/j.commatsci.2015.05.006>
- Liu, Y., Xu, Z., 2014. Multimodal and self-healable interfaces enable strong and tough graphene-derived materials. *J. Mech. Phys. Solids*. <https://doi.org/10.1016/j.jmps.2014.05.006>
- Meng, Q., Li, B., Li, T., Feng, X.Q., 2017. A multiscale crack-bridging model of cellulose

- nanopaper. *J. Mech. Phys. Solids*. <https://doi.org/10.1016/j.jmps.2017.03.004>
- Miyazaki, H.T., Tomizawa, Y., Saito, S., Sato, T., Shinya, N., 2000. Adhesion of micrometer-sized polymer particles under a scanning electron microscope. *J. Appl. Phys.*  
<https://doi.org/10.1063/1.1288006>
- Na, S.R., Wang, X., Piner, R.D., Huang, R., Willson, C.G., Liechti, K.M., 2016. Cracking of Polycrystalline Graphene on Copper under Tension. *ACS Nano*.  
<https://doi.org/10.1021/acsnano.6b05101>
- Nairn, J.A., 1997. On the use of shear-lag methods for analysis of stress transfer in unidirectional composites. *Mech. Mater.* [https://doi.org/10.1016/S0167-6636\(97\)00023-9](https://doi.org/10.1016/S0167-6636(97)00023-9)
- Needleman, A., 1990. An analysis of tensile decohesion along an interface. *J. Mech. Phys. Solids*. [https://doi.org/10.1016/0022-5096\(90\)90001-K](https://doi.org/10.1016/0022-5096(90)90001-K)
- Park, K., Paulino, G.H., 2013. Cohesive Zone Models: A Critical Review of Traction-Separation Relationships Across Fracture Surfaces. *Appl. Mech. Rev.*  
<https://doi.org/10.1115/1.4023110>
- Qian, D., Wagner, G.J., Liu, W.K., Yu, M.F. and Ruoff, R.S., 2002. Mechanics of carbon nanotubes. *Appl. Mech. Rev.* <https://doi.org/10.1115/1.1490129>
- Qin, Q., Zhu, Y., 2011. Static friction between silicon nanowires and elastomeric substrates. *ACS Nano*. <https://doi.org/10.1021/nn202343w>
- Rogers, J.A., Someya, T., Huang, Y., 2010. Materials and mechanics for stretchable electronics. *Science (80-. )*. <https://doi.org/10.1126/science.1182383>
- Ryu, S.Y., Xiao, J., Park, W. Il, Son, K.S., Huang, Y.Y., Paik, U., Rogers, J.A., 2009. Lateral buckling mechanics in silicon nanowires on elastomeric substrates. *Nano Lett.*  
<https://doi.org/10.1021/nl901450q>

- Safaei, M., Sheidaei, A., Baniassadi, M., Ahzi, S., Mosavi Mashhadi, M., Pourboghrat, F., 2015. An interfacial debonding-induced damage model for graphite nanoplatelet polymer composites. *Comput. Mater. Sci.* <https://doi.org/10.1016/j.commatsci.2014.08.036>
- She, H., Malotky, D., Chaudhury, M.K., 1998. Estimation of Adhesion Hysteresis at Polymer/Oxide Interfaces Using Rolling Contact Mechanics. *Langmuir*. <https://doi.org/10.1021/la971061m>
- Strus, M.C., Lahiji, R.R., Ares, P., López, V., Raman, A., Reifenberger, R., 2009. Strain energy and lateral friction force distributions of carbon nanotubes manipulated into shapes by atomic force microscopy. *Nanotechnology*. <https://doi.org/10.1088/0957-4484/20/38/385709>
- Su, T., Liu, J., Terwagne, D., Reis, P.M., Bertoldi, K., 2014. Buckling of an elastic rod embedded on an elastomeric matrix: Planar vs. non-planar configurations. *Soft Matter*. <https://doi.org/10.1039/c4sm00952e>
- Sun, Y., Rogers, J.A., 2007. Structural forms of single crystal semiconductor nanoribbons for high-performance stretchable electronics. *J. Mater. Chem.* <https://doi.org/10.1039/b614793c>
- Wagner, H.D., Eitan, A., 1990. Interpretation of the fragmentation phenomenon in single-filament composite experiments. *Appl. Phys. Lett.* <https://doi.org/10.1063/1.103012>
- Wang, G., Dai, Z., Liu, L., Hu, H., Dai, Q., Zhang, Z., 2016. Tuning the Interfacial Mechanical Behaviors of Monolayer Graphene/PMMA Nanocomposites. *ACS Appl. Mater. Interfaces*. <https://doi.org/10.1021/acsami.6b03069>
- Xu, F., Durham, J.W., Wiley, B.J., Zhu, Y., 2011a. Strain-release assembly of nanowires on stretchable substrates. *ACS Nano*. <https://doi.org/10.1021/nn103183d>
- Xu, F., Lu, W., Zhu, Y., 2011b. Controlled 3D buckling of silicon nanowires for stretchable

- electronics. ACS Nano. <https://doi.org/10.1021/nm103189z>
- Yao, S., Zhu, Y., 2015. Nanomaterial-enabled stretchable conductors: Strategies, materials and devices. Adv. Mater. <https://doi.org/10.1002/adma.201404446>
- Zhao, Y., Li, J., Cao, Y.P., Feng, X.Q., 2016. Buckling of an elastic fiber with finite length in a soft matrix. Soft Matter. <https://doi.org/10.1039/c5sm02284c>
- Zhu, Y., 2017. Mechanics of Crystalline Nanowires: An Experimental Perspective. Appl. Mech. Rev. <https://doi.org/10.1115/1.4035511>
- Zhu, Y., Liechti, K.M., Ravi-Chandar, K., 2009a. Direct extraction of rate-dependent traction-separation laws for polyurea/steel interfaces. Int. J. Solids Struct. <https://doi.org/10.1016/j.ijsolstr.2008.08.019>
- Zhu, Y., Xu, F., Qin, G., Fung, W.Y., Lu, W., 2009b. Mechanical properties of vapor - Liquid - Solid synthesized silicon nanowires. Nano Lett. <https://doi.org/10.1021/nl902132w>

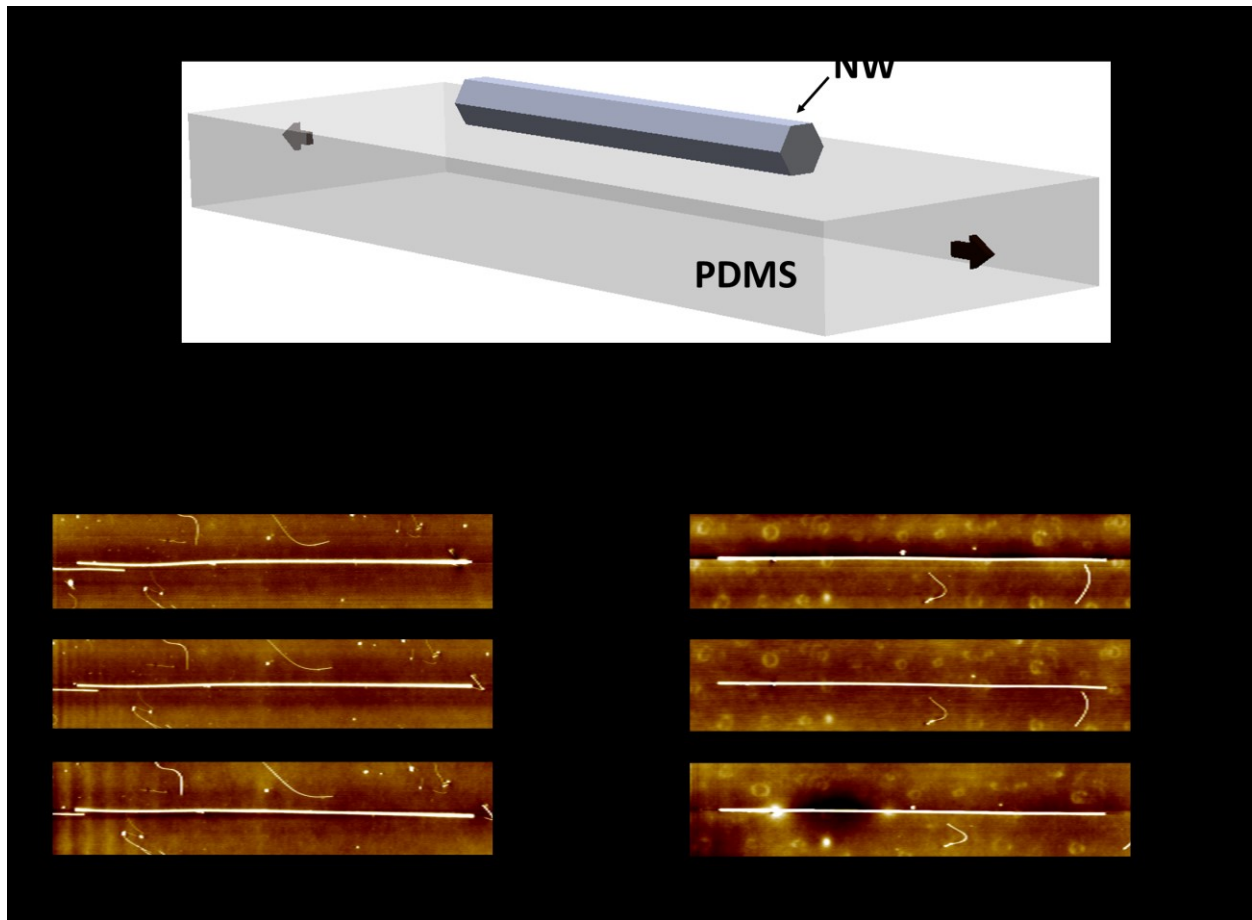


**Fig. 1.** (a) Schematic of the experimental setup with a Si nanowire (NW) on top of PDMS substrate, (b) AFM images of a Si nanowire on top of as-prepared PDMS, and (c) AFM images of a Si nanowire on top of UVO-treated PDMS.

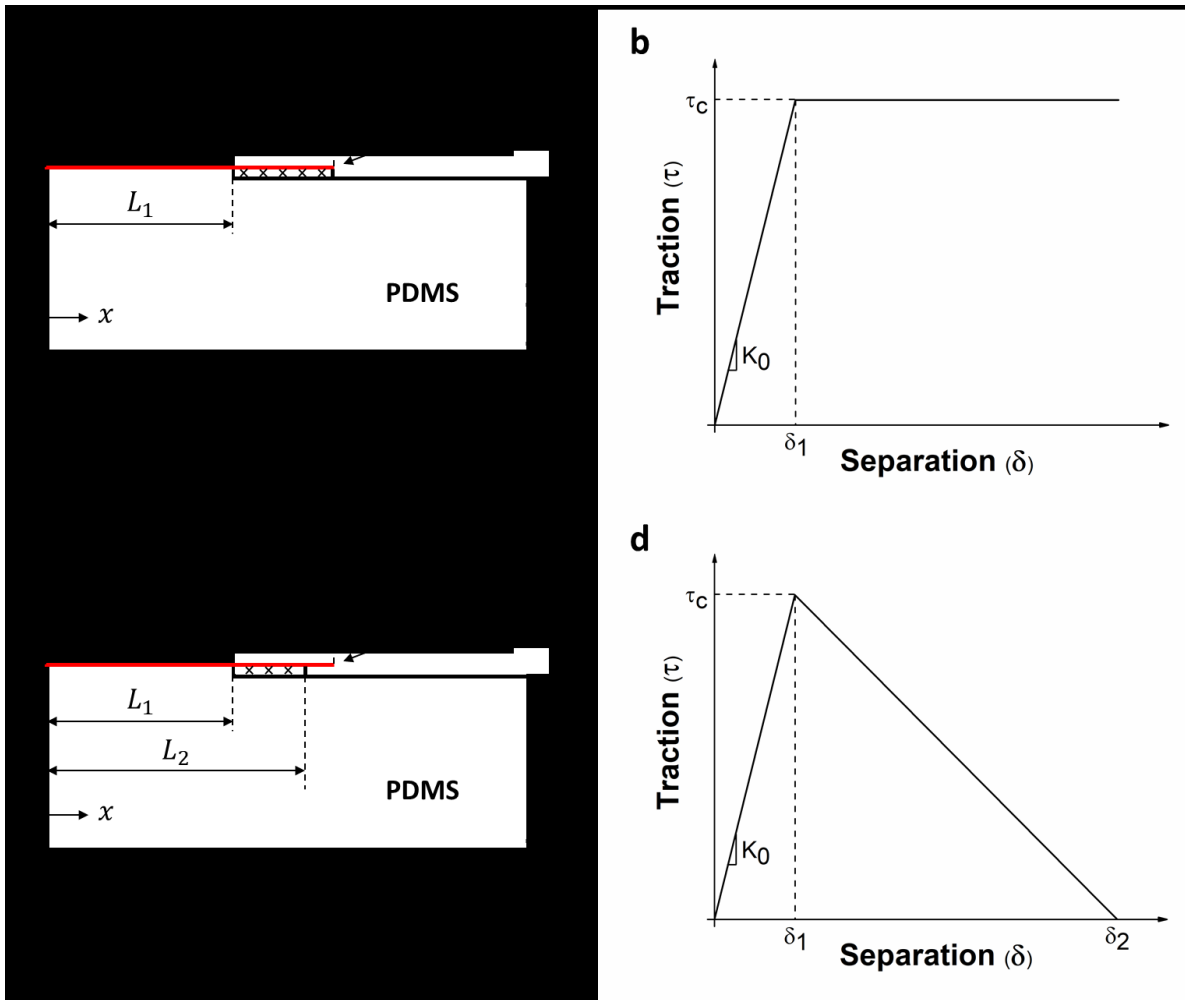


**Fig. 2.** (a) Schematic of nonlinear shear-lag model and (b) corresponding traction-separation law; (c) schematics of cohesive shear-lag model and (d) corresponding traction-separation law.

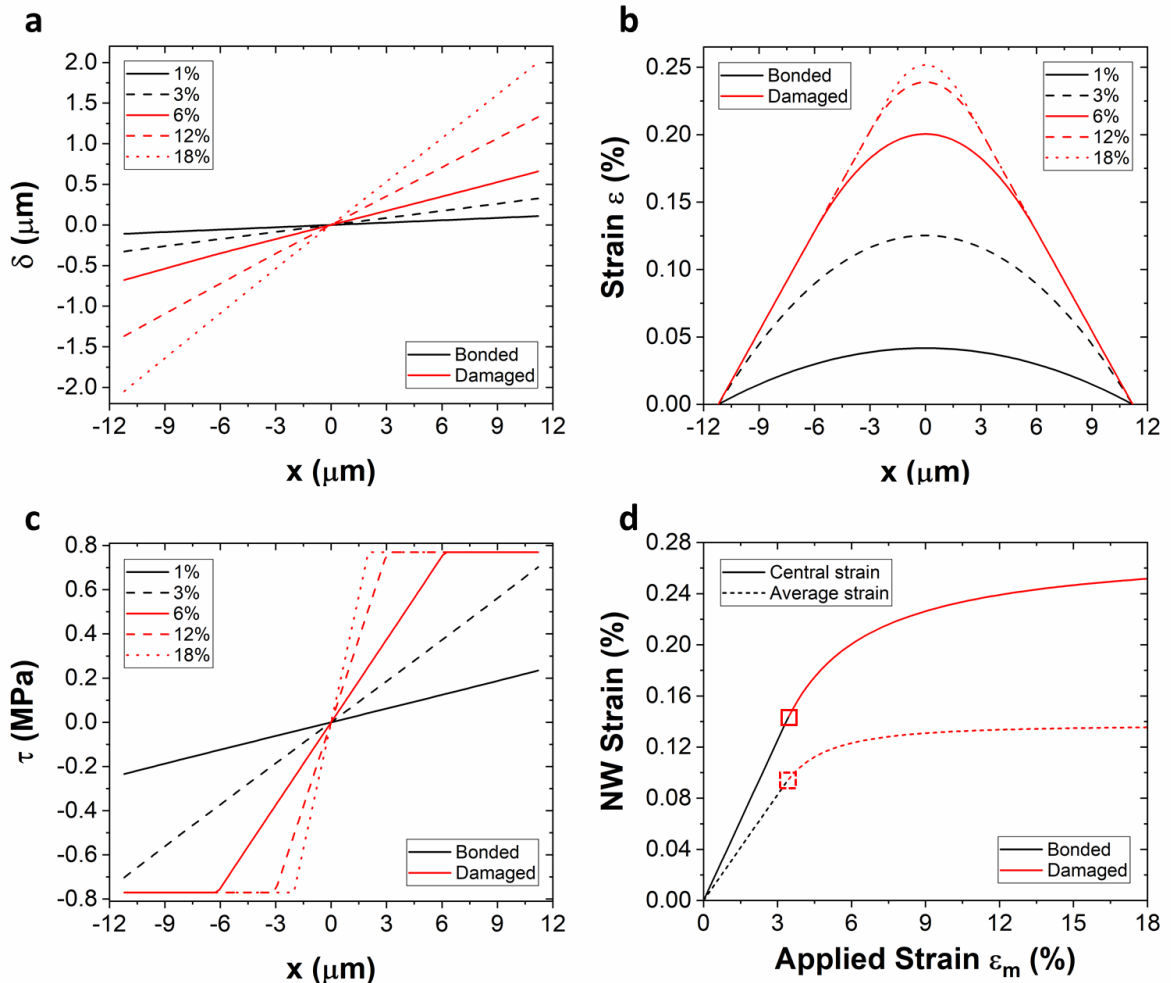


**Fig. 3.** Nonlinear shear-lag model results for  $\epsilon_m$  varying from 1 to 18% with  $L = 11.2 \mu\text{m}$ ,  $a = 10 \text{ nm}$ , and  $\beta = 0.026 \text{ m}^{-1}$ : (a) relative displacement, (b) NW axial strain, (c) interfacial shear stress along the nanowire length, and (d) nanowire center strain and average strain vs. substrate strain (square dots mark the bonded-damaged transition).

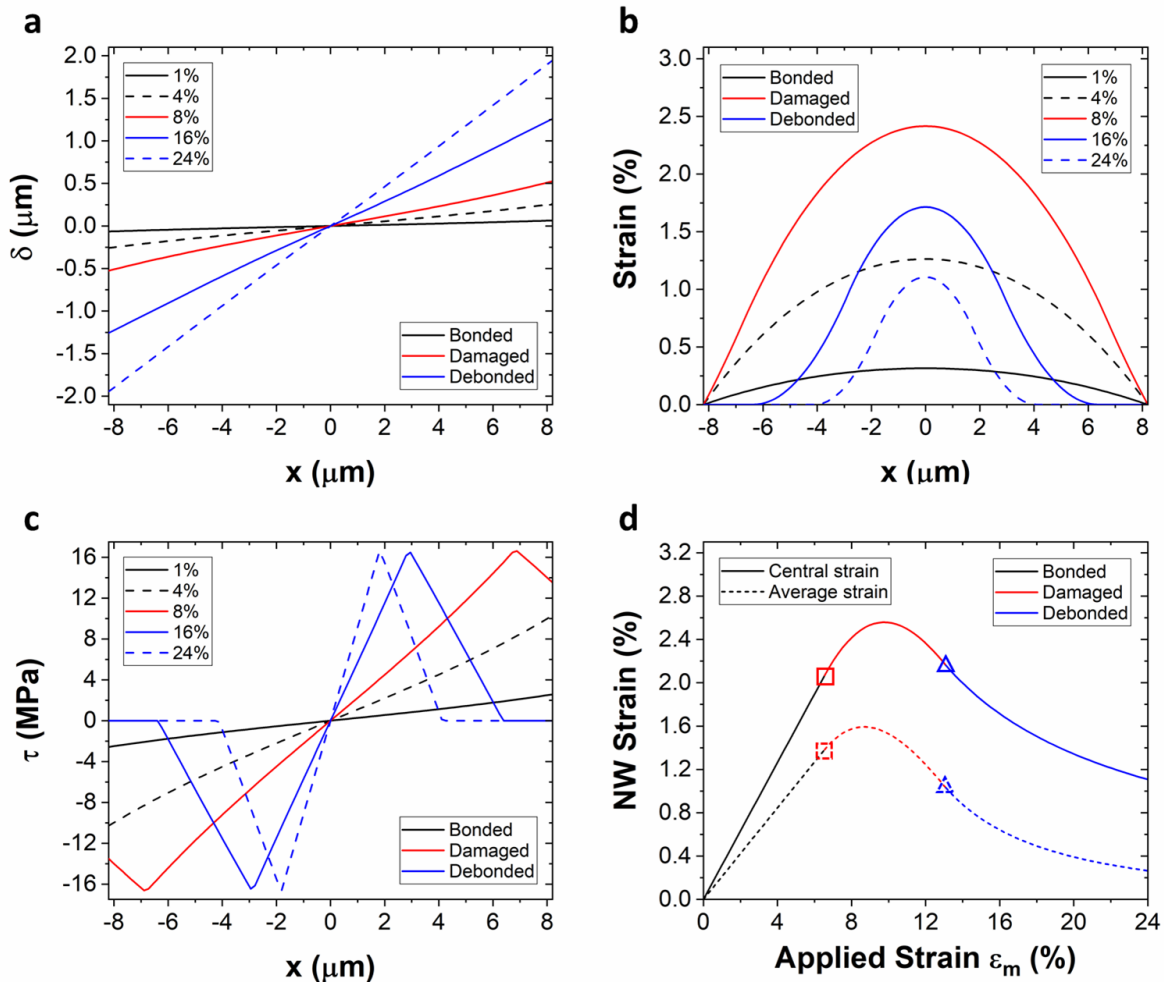


**Fig. 4.** Cohesive shear-lag model results for  $\varepsilon_m$  varying from 1 to 24% when  $L = 8.2 \mu\text{m}$ ,  $a = 10 \text{ nm}$ , and  $\beta = 0.113 \text{ m}^{-1}$ : (a) relative displacement, (b) NW axial strain, (c) interfacial shear stress along the nanowire length, and (d) nanowire center strain and average strain vs. substrate strain (square dots mark the bonded-damaged transition and triangle dots mark the damaged-debonded transition).

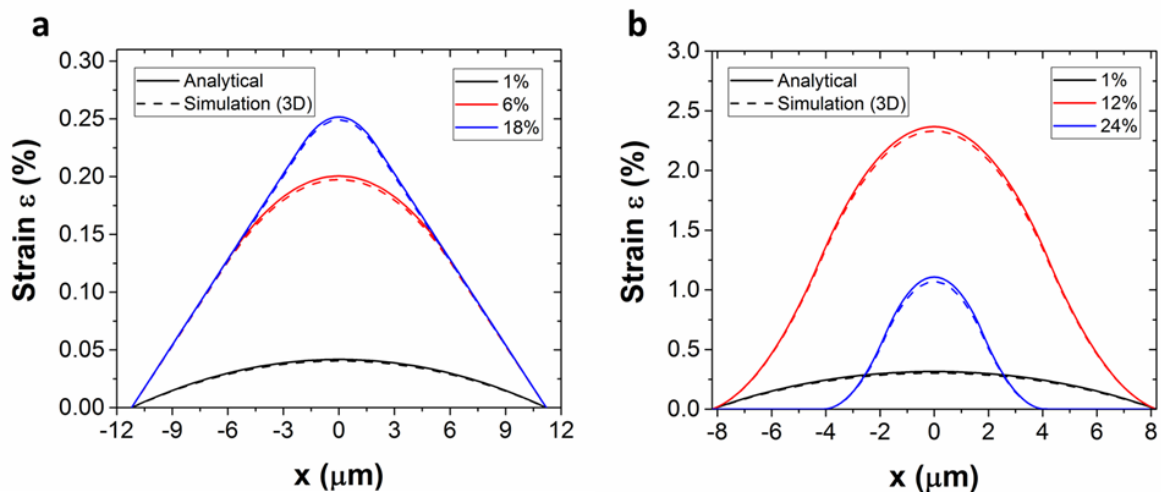


**Fig. 5.** Normal strain along the nanowire length predicted by analytical modeling and 3D FEA, for (a) as-prepared PDMS and (b) UVO-treated PDMS. In both cases the nanowire diameter is 10 nm.

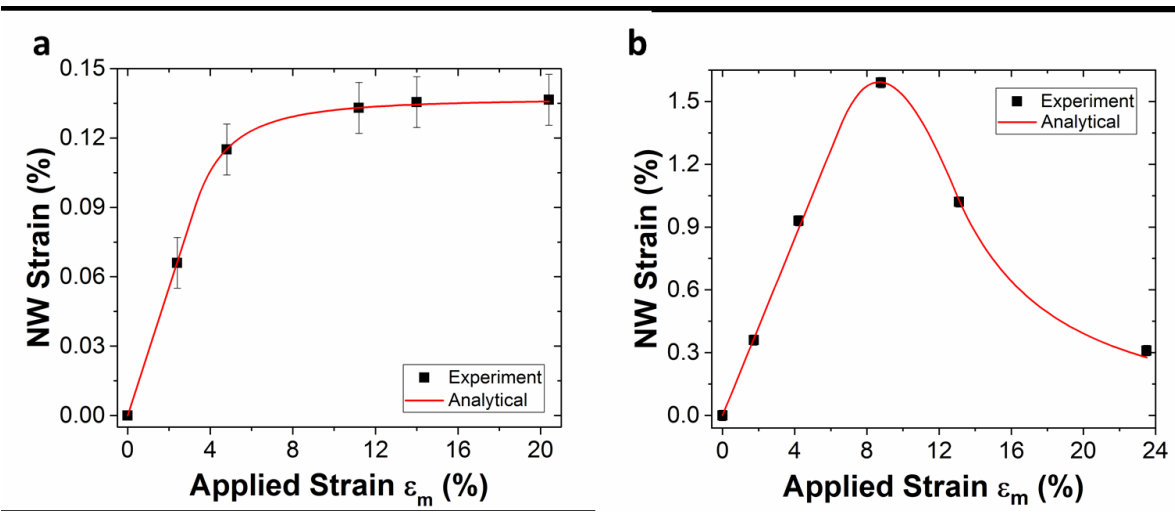


**Fig. 6.** Fitting experimental data for (a) as-prepared PDMS using nonlinear shear-lag model and for (b) UVO-treated PDMS using cohesive shear-lag model.

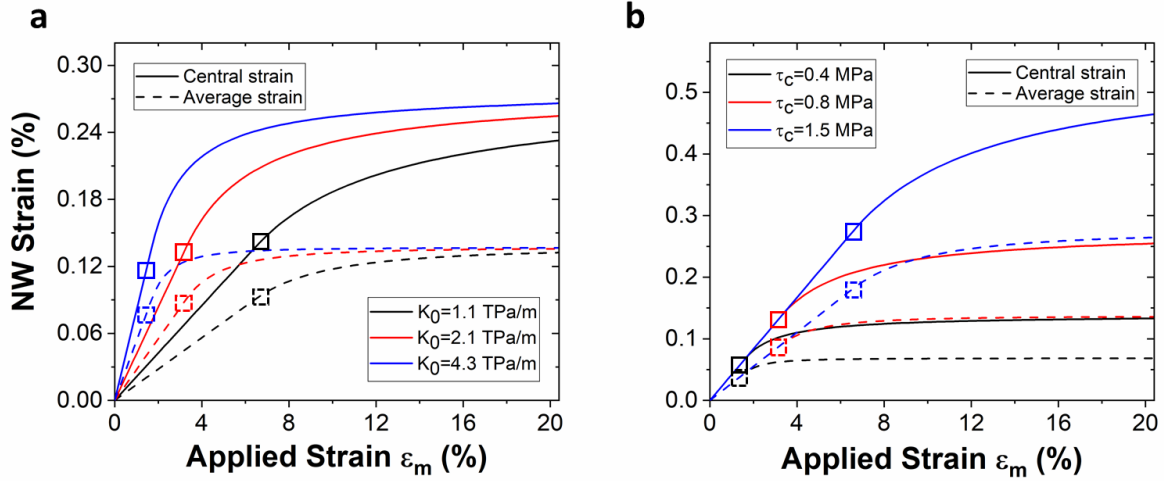


**Fig. 7.** Parametric study of the nonlinear shear-lag model (as-prepared PDMS) on the nanowire center and average strain: (a) effect of  $K_0$  and (b) effect of  $\tau_c$  (square dots mark the bonded-damaged transition).

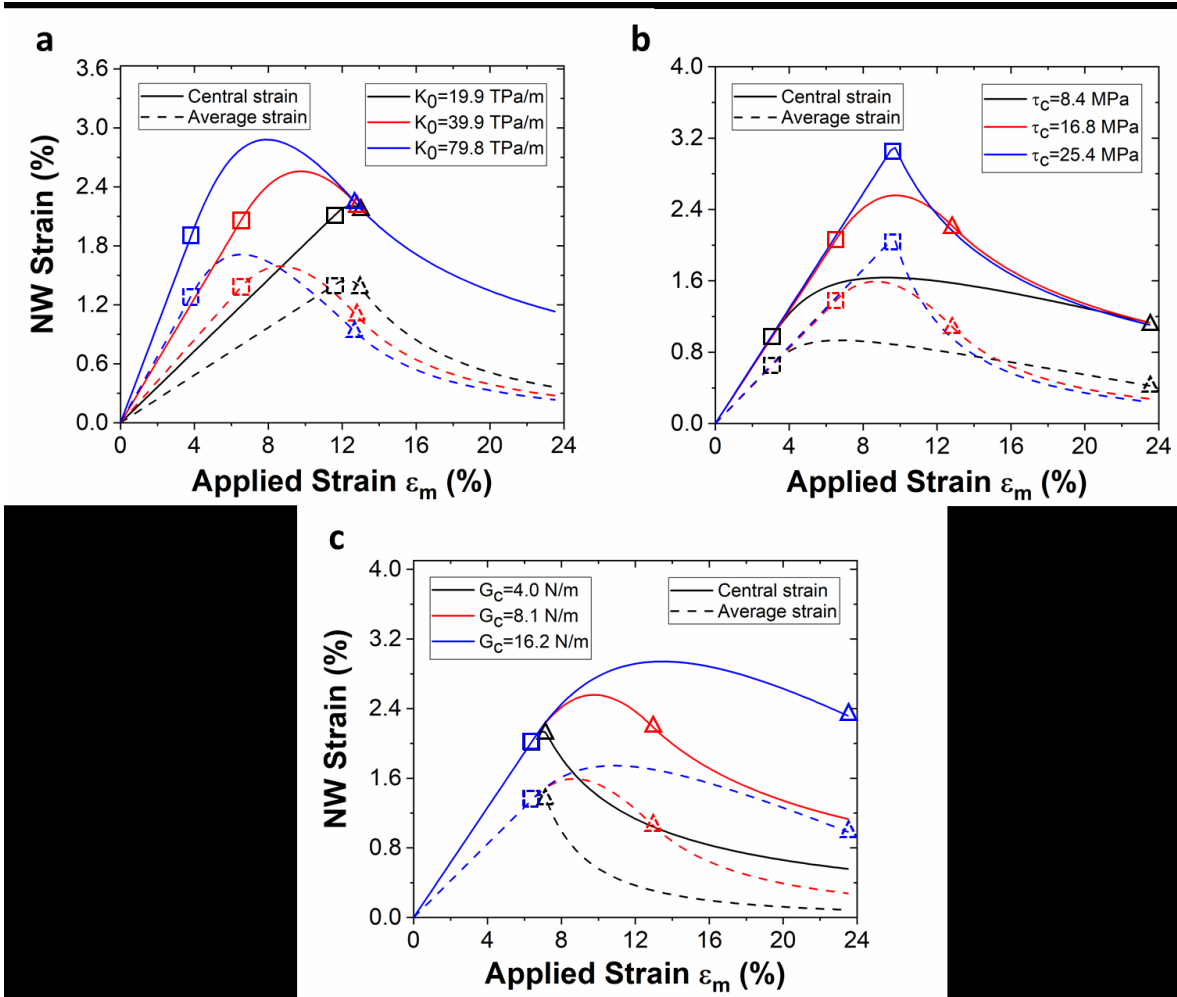


**Fig. 8.** Parametric study of the cohesive shear-lag model (UVO-treated PDMS) on the nanowire center and average strain: (a) effect of  $K_0$ , (b) effect of  $\tau_c$ , and (c) effect of  $G_c$  (square dots mark the bonded-damaged transition and triangle dots mark the damaged-debonded transition).

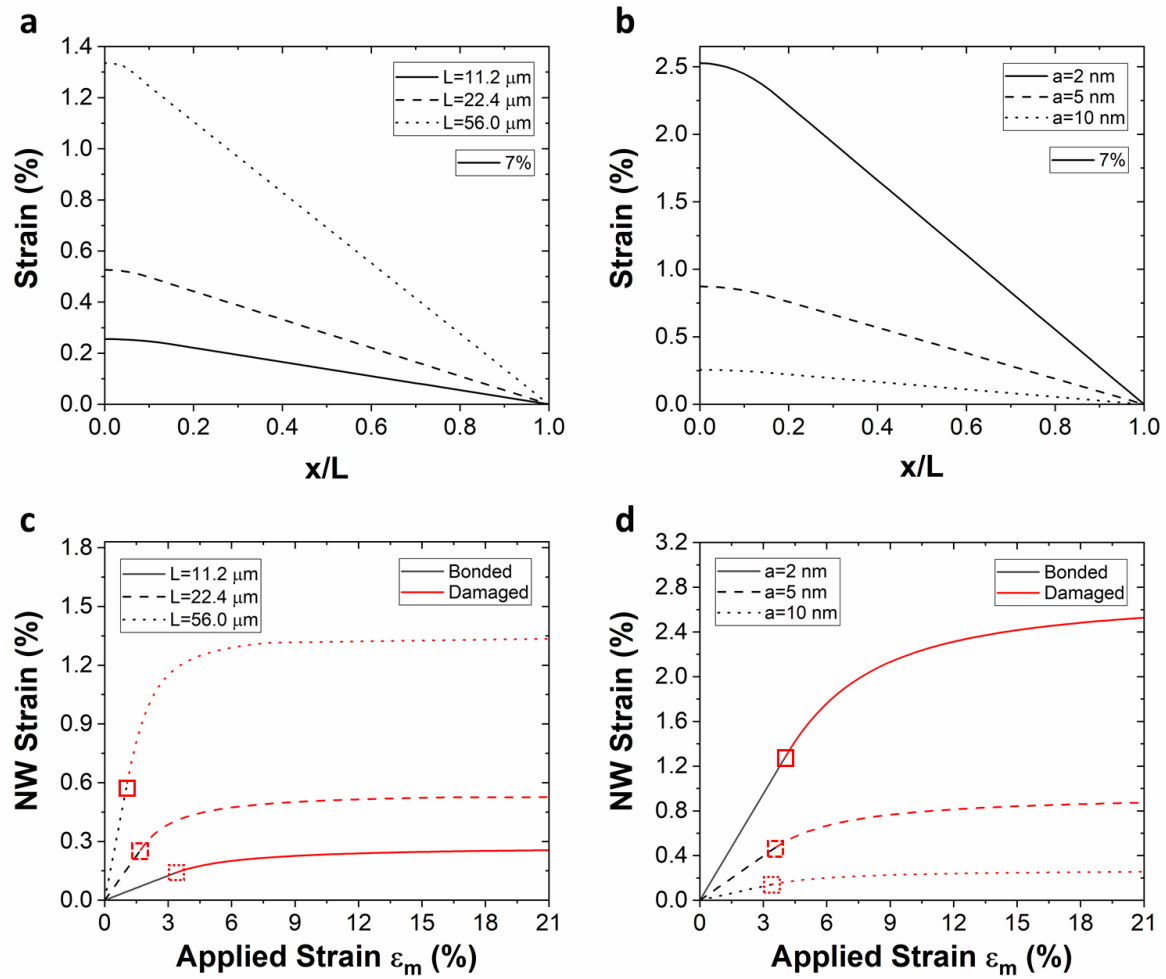


**Fig. 9.** Parametric study of the nonlinear shear-lag model (as-prepared PDMS) on the strain along the nanowire length: (a) effect of length  $L$  and (b) effect of radius  $a$ . Parametric study on the nanowire maximum (center) strain: (c) effect of length  $L$  and (d) effect of radius  $a$ .

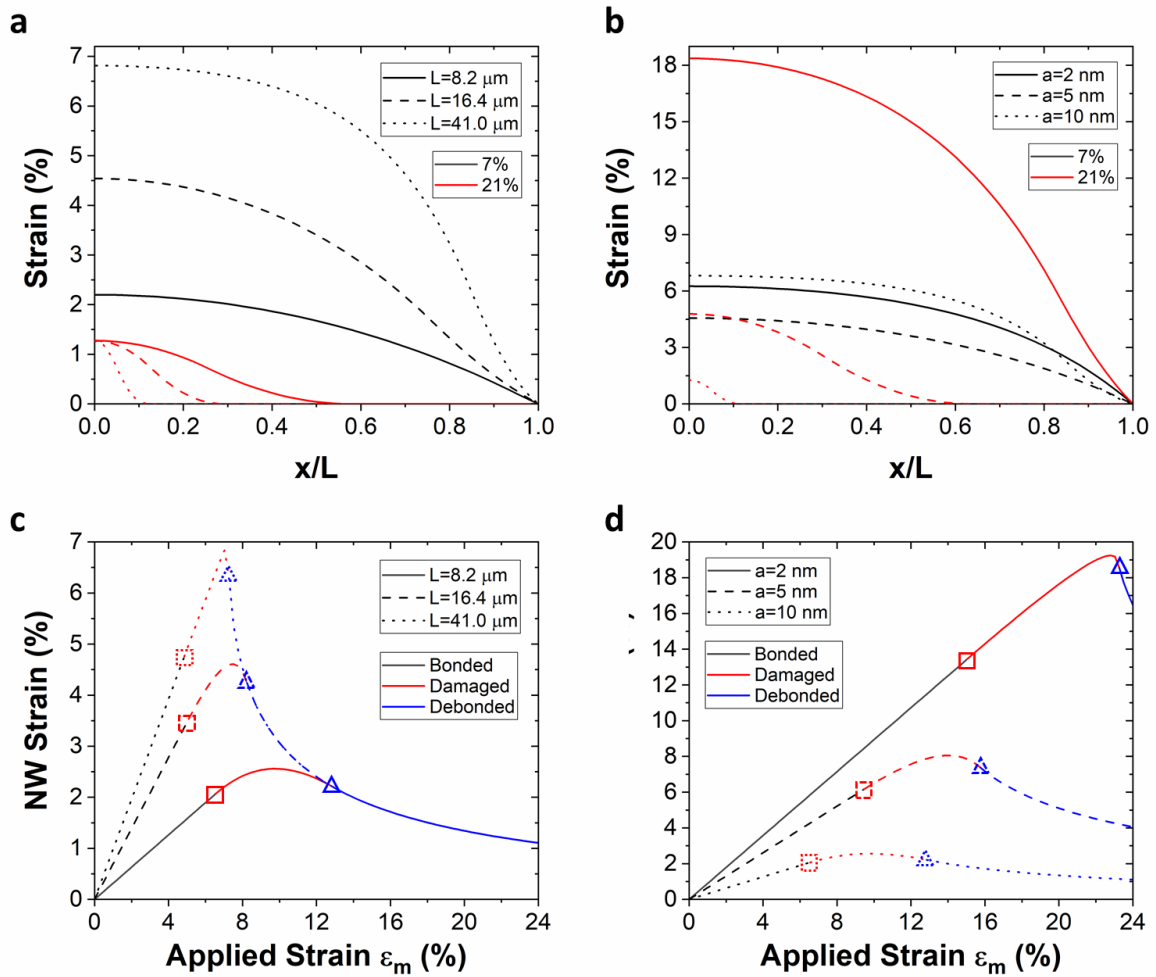


**Fig. 10.** Parametric study of the cohesive shear-lag model (UVO-treated PDMS) on the strain along the NW length: (a) effect of length  $L$  and (b) effect of radius  $a$ . Parametric study on the nanowire maximum (center) strain: (c) effect of length  $L$  and (d) effect of radius  $a$ .

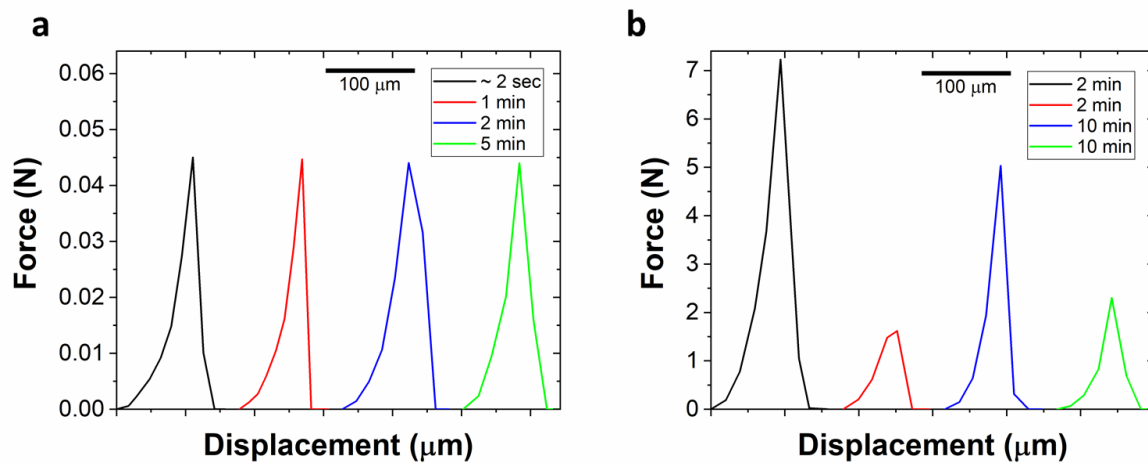


**Fig. A.1.** Adhesion forces measured for (a) as-prepared PDMS sample and (b) 20 min UVO-treated PDMS sample. For each case, the tests were carried out following the order from left to right.